

Mass ejection by pulsational pair instability in very massive stars and implications for luminous supernovae

Takashi Yoshida^{1*}, Hideyuki Umeda¹, Keiichi Maeda^{2,3}, and Tatsuo Ishii⁴

¹*Department of Astronomy, Graduate School of Science, University of Tokyo, Tokyo 113-0033, Japan*

²*Department of Astronomy, Graduate School of Science, Kyoto University, Kyoto 606-8502, Japan*

³*Kavli Institute for the Physics and Mathematics of the Universe (WPI), University of Tokyo, Chiba 277-8583, Japan*

⁴*Department of General Systems Studies, Graduate School of Arts and Sciences, University of Tokyo, Tokyo 153-8902, Japan*

Accepted 2015 December 22, Received 2015 December 11; in original form 2015 November 5

ABSTRACT

Massive stars having a CO core of $\sim 40\text{--}60 M_{\odot}$ experience pulsational pair-instability (PPI) after carbon-burning. This instability induces strong pulsations of the whole star and a part of outer envelope is ejected. We investigate the evolution and mass ejection of metal-poor very massive stars which experience PPI. We use stellar models with initial masses of 140, 200, and 250 M_{\odot} and the metallicity $Z = 0.004$. Their masses decrease to 54.09, 58.65, and 61.03 M_{\odot} before the neon-burning owing to mass-loss and He mass fraction at the surface becomes about 20 per cent. During the PPI period of $\sim 1\text{--}2000$ yr, they experience six, four, and three pulsations, respectively. The larger CO-core model has the longer PPI period and ejects the larger amount of mass. Since almost all surface He has been lost by the pulsations, these stars become Type Ic supernovae if they explode. Light curves during the PPI stage and supernovae are investigated and are implicated in luminous supernovae. The luminosity created by the interaction of different PPI ejecta becomes $M_{\text{bol}} \sim -16$ to -20 . The interaction between the circumstellar shell ejected by PPI and the supernova ejecta can be more luminous. These luminous transients could be an origin of Type I superluminous supernovae and supernovae with precursor.

Key words: stars: evolution – stars: massive – stars: mass-loss – supernovae: general – supernovae: individual: SN 2006jc – stars: Wolf–Rayet

1 INTRODUCTION

Massive stars in a certain mass range experience strong pulsations by an instability induced by electron-positron pair-creation during O- and Si-burning. This pulsation event is called as pulsational pair-instability (PPI). The pulsation mechanism is the same as pair-instability supernova (PISN) but the released energy is too small to explode the whole star. The mass range of the corresponding CO core is about $40\text{--}60 M_{\odot}$ (Heger & Woosley 2002; Umeda & Nomoto 2002, 2008; Waldman 2008), which is smaller than that of the PISN progenitors, $\sim 60\text{--}130 M_{\odot}$ (e.g. Heger & Woosley 2002; Umeda & Nomoto 2002; Takahashi et al. 2015). In metal-poor stars, the mass range strongly depends on mass-loss rate. A part of very massive stars with the metallicity $Z \lesssim 0.004$ experience the PPI (Yoshida & Umeda 2011; Yoshida, Okita & Umeda 2014). Recently, evolution of metal-poor very mas-

sive stars has been investigated (e.g. Langer et al. 2007; Yungelson, et al. 2008; Yoshida & Umeda 2011; Yusof, et al. 2013; Yoshida, Okita & Umeda 2014) for superluminous supernovae (SLSNe) (Smith et al. 2007; Gal-Yam et al. 2009) and new findings of very massive stars (Crowther et al. 2010).

Strong pulsations by the PPI induce eruptive mass-loss. The mass ejection from the H-rich envelope and He-layer has been investigated in Woosley, Blinnikov, & Heger (2007). The case of the first pulsation in rotating He stars and CO stars has been examined in Chatzopoulos & Wheeler (2012). The collisions of the ejected matter to the earlier ejecta induce brilliant optical transients. The brilliant events by the collision during the PPI have been numerically shown in Woosley, Blinnikov, & Heger (2007). The luminosity of the evaluated light curve can be similar to SLSNe.

SLSNe have recently been found as very bright supernovae (SNe) ($M_{\text{peak}} < -21$; Gal-Yam 2012). SLSNe of Type I and Type II (SLSNe-I and SLSNe-II) were identified as SNe Ic and SNe IIn, respectively, and their light curves

* E-mail: tyoshida@astron.s.u-tokyo.ac.jp

have large diversity and some of them indicate fast declines (e.g. Quimby et al. 2007, 2011). SLSNe-R show slow decline and are considered to be powered by the radioactive decays of ^{56}Ni and ^{56}Co (Gal-Yam et al. 2009; Gal-Yam 2012). However, emission processes and explosion mechanism of these SNe are not still clarified. Several possibilities of emission processes such as the interaction between circumstellar medium (CSM) released by eruptive mass-loss and the SN ejecta, mass ejection from nascent magnetars (e.g. Maeda et al. 2007; Kasen & Bildsten 2010), PISNe (Gal-Yam et al. 2009), and core-collapse (CC) SNe after PPI (Moriya et al. 2010; Yoshida, Okita & Umeda 2014) have been proposed. Another class of candidates of PPI events are bright optical transients which were found in a few years before SN explosion for some SNe such as SN 2006jc (Pastorello et al. 2007) and SN 2009ip (Pastorello et al. 2013). The transients would be powered by outbursts, and a part of the envelope would have been removed. This would be related to the PPI of very massive stars.

We investigate the mass ejection by the PPI of massive Wolf-Rayet (WR) stars evolved from metal-poor very massive stars. We also investigate the time evolution of resulting optical events during the PPI stage and SN explosions of massive WR stars. The massive WR stars are more compact than red giants having H-rich envelope. The surface composition of these stars mainly consists of C and O, and a small amount of He is also included. Therefore, these transients and SN explosions will be observed as SNe Ib or SNe Ic. We note that whether these WR stars explode as SNe has not been clarified. If these stars collapse and do not explode, the luminous optical event caused by SNe will not be seen.

We organize this paper as follows. We describe the models for stellar evolution and the mass ejection by PPI in Section 2. Then, we show details for the stellar evolution and mass ejection during the PPI stage of 140, 200, and 250 M_{\odot} models. We briefly show the characteristics of their SN explosions with the explosion energy of 10^{51} erg and 10^{52} erg in Section 3. In Section 4, we show light curves of optical transients during the PPI stage and SN explosions. We discuss characteristics of PPI in our models in Section 5. We also discuss observations of the optical transients with precursors and SLSNe from a viewpoint of the PPI and SN explosions of very massive stars. We summarize this study in Section 6.

2 STELLAR EVOLUTION AND MASS EJECTION DURING PPI STAGE

We pursue the evolution and mass ejection during PPI stage of 140, 200, and 250 star models using a stellar evolution code and a hydrodynamic code. First, we describe details for the calculation method in this stage. Then, we show the results of the evolution and mass ejection. These stars pulsate several times by pair instability and eject their outer region by each pulsation. The total mass and surface composition change by the pulsations. We also present the stellar mass dependence of detailed evolution.

Table 1. The total mass M_{total} , CO core mass M_{CO} , and the surface mass fractions of He ($X_{\text{S}}(\text{He})$), C ($X_{\text{S}}(\text{C})$), and O ($X_{\text{S}}(\text{O})$) of the stellar models.

M_{ZAMS} (M_{\odot})	M_{total} (M_{\odot})	M_{CO} (M_{\odot})	$X_{\text{S}}(\text{He})$	$X_{\text{S}}(\text{C})$	$X_{\text{S}}(\text{O})$
140	54.09	48.09	0.192	0.415	0.386
200	58.65	52.28	0.198	0.412	0.384
250	61.03	53.95	0.193	0.407	0.393

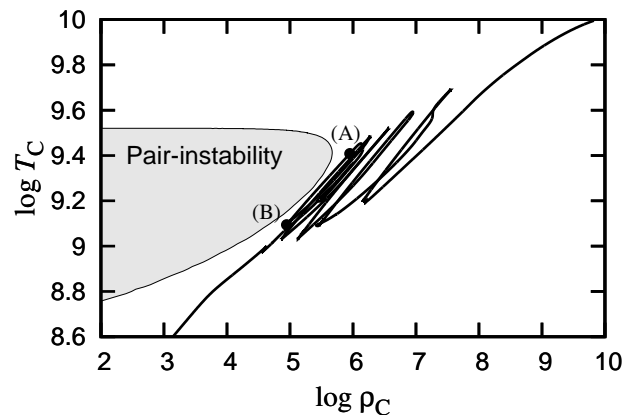


Figure 1. The evolution of the 140 M_{\odot} model on the plane of $\log \rho_{\text{C}} - \log T_{\text{C}}$ after He core burning. The shaded region shows unstable region against electron-positron pair instability. Details for points (A) and (B) are explained in text.

2.1 Calculation method of stellar evolution and mass ejection during PPI stage

In order to calculate advanced stages of very massive stars, we use the stellar structure calculated in Yoshida, Okita & Umeda (2014). We take three models with the initial masses of 140, 200, and 250 M_{\odot} and the metallicity of $Z = 0.004$ as the initial structure. These stars lose H envelope and He layer and evolve to WO stars. The total mass, CO core mass, and surface composition after the C-burning are listed in Table 1. The CO-core mass is defined as the largest mass coordinate satisfying He mass fraction smaller than 10^{-3} . We calculate the evolution after the C burning to the onset of the CC using the stellar evolution code adopted in Yoshida, Okita & Umeda (2014). The acceleration term is included in this code. Note that exact expression of energy generation in the formulation of stellar evolution is discussed in Takahashi et al. (2015). This expression has not been included in this study.

We calculate the evolution during PPI stage using the stellar evolution code and a PPM hydrodynamic code (e.g. Colella & Woodward 1984; Umeda & Nomoto 2005) as follows. This is because it is difficult to solve unbound surface structure during the PPI mass ejection using the stellar evolution code.

We describe the calculation method using the second pulsation of the 140 M_{\odot} star model as an example. Fig. 1 shows the evolutionary track of the 140 M_{\odot} star model on the plane of $\log \rho_{\text{C}}$ (the central density) and $\log T_{\text{C}}$ (the central temperature). Two points (A) and (B) in the second

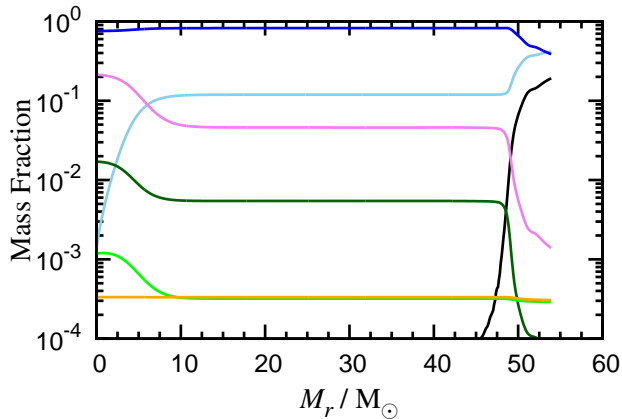


Figure 2. Mass fraction distribution of the $140 M_{\odot}$ model after the C-burning at $\log T_C = 9.14$. Black, sky-blue, blue, purple, dark-green, green, and orange lines indicate the mass fractions of ${}^4\text{He}$, ${}^{12}\text{C}$, ${}^{16}\text{O}$, ${}^{20}\text{Ne}$, ${}^{24}\text{Mg}$, intermediate-mass elements (Si-Sc), and Fe-peak elements (Ti-), respectively.

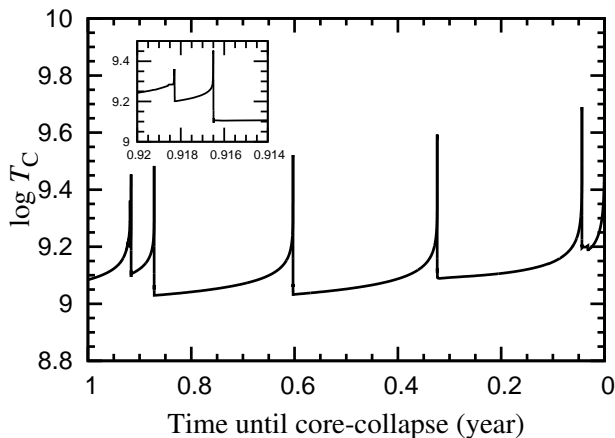


Figure 3. Time evolution of the central temperature $\log T_C$ of the $140 M_{\odot}$ model during PPI stage. The small figure shows the central temperature between 0.92 yr and 0.914 yr.

pulsation are assigned. First, we calculate the stellar evolution passing through points (A) and (B) without mass-loss by the PPI using the stellar evolution code.

Next, using the PPM code, we calculate the mass ejection of the star for about 10^4 s, corresponding to the period until the mass ejection is almost completed. The initial structure is set to be the structure at the time when the star has the maximum total energy during the pulsation (point (A) in the second pulsation). During the expansion, outermost region of the star accelerates and exceeds escape velocity. Thus, the mass exceeding the escape velocity is considered as the ejected mass.

Then, we restart the stellar evolution calculation from the time when the central temperature is almost minimal (point (B) in the second pulsation). We artificially reduce stellar mass with a constant mass-loss rate evaluated in the previous hydrodynamic calculation. The mass-loss continues until the lost mass is equal to the ejected mass obtained from the hydrodynamic calculation. After several pulsations, the

star forms an Fe core and collapses. We stop the calculation of the stellar evolution when the central temperature reaches 10^{10} K.

2.2 Stellar evolution during PPI stage

First, we show the evolution of the $140 M_{\odot}$ model after the C-burning. Fig. 2 shows the mass fraction distribution after the C-burning. The central temperature is $\log T_C = 9.14$. The main component at the centre is O, Ne, and Mg. The mass fraction of Si also increases. The central C burning occurs radiatively. The O/C/Ne layer is in the range of ~ 6 – $48 M_{\odot}$ in the mass coordinate. The surface component is mainly O and C, and 19 per cent ${}^4\text{He}$ by mass fraction remains as shown in Table 1.

The time evolution on the plane of the central temperature and density is shown in Fig. 1. This star pulsates six times by pair instability. The evolution line passes close to the right of the pair-instability region. After the temperature minimal in each pulse, the slope of the evolution line becomes less steep. In this stage, the star contracts quasi-statically and neutrino cooling becomes more effective. As the contraction timescale becomes shorter, the evolution line becomes steeper.

Fig. 3 shows the time evolution of the central temperature. The ejected mass and the kinetic energy of the ejecta in each pulsation are shown in Table 2. The PPI period, i.e., the period from the central carbon exhaustion to the onset of the CC, is about 1 yr. After 6.2 d from the central carbon exhaustion, the contraction changes to dynamical. The dynamical contraction increases the temperature in a short timescale and causes the central Ne/O-burning and shell C-burning. This contraction stops at the central temperature of $\log T_C = 9.36$ and the star expands by rapid Ne/O-burning. The expansion continues until $\log T_C = 9.20$. Fig. 4 (a) shows the mass fraction distribution after the 1st pulsation. The mass fractions of ${}^{16}\text{O}$, ${}^{24}\text{Mg}$, and ${}^{28}\text{Si}$ are 0.84, 0.07, and 0.07 at the centre, respectively. The O/Ne layer forms in $M_r \sim 6.7$ – $16 M_{\odot}$. The chemical composition outside $\sim 20 M_{\odot}$ is not affected by this pulsation. This expansion is too weak to erupt the CO-rich envelope. Then, the next contraction proceeds for 15 hr.

The second pulsation raises the central temperature up to $\log T_C = 9.45$. Then, the central temperature decreases to $\log T_C = 9.09$ by the expansion. The central ${}^{16}\text{O}$ is burned to intermediate elements such as Si and S. The mass fraction of ${}^{16}\text{O}$ at the centre decreases to 0.16 (see Fig. 4 (b)). The O/Mg/Si layer is formed in the region inside about $10 M_{\odot}$. A part of the O/Ne layer and the outer O/Si layer mix, thus, the composition in $M_r \lesssim 30 M_{\odot}$ also changes. The mass fractions of Ne and C in this region are roughly equal. In this pulsation, the outer region of $0.25 M_{\odot}$ is ejected through the rapid expansion. The quasi-static period in the next contraction is about 16 d.

In the third pulsation, the central temperature rises up to $\log T_C = 9.48$. After the expansion, the central temperature decreases to $\log T_C = 9.03$. The O mass fraction at the centre decreased to 2×10^{-3} and the main component becomes intermediate nuclei such as Si and S (see Fig. 4 (c)). The outer boundary of the surrounding O/Mg/Si layer becomes about $11 M_{\odot}$. In the region inside $38 M_{\odot}$, the Ne mass fraction becomes larger than C owing to shell C-burning and

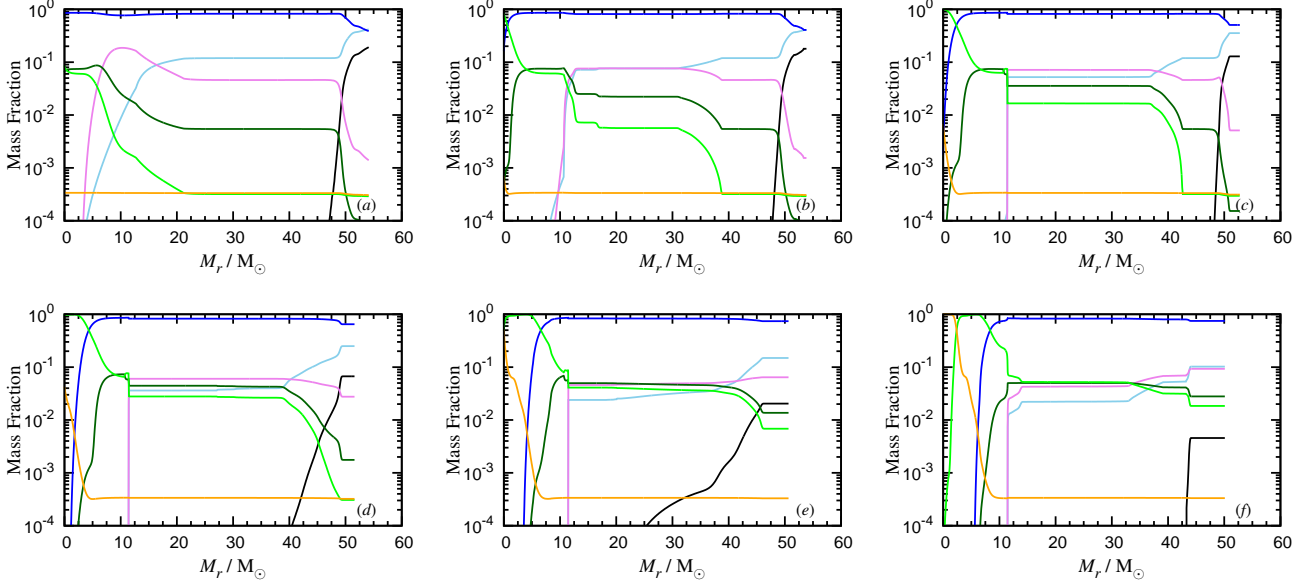


Figure 4. Mass fraction distribution of the $140 M_{\odot}$ model after the first (a), second (b), third (c), fourth (d), fifth (e), and sixth (f) pulses. Black, sky-blue, blue, purple, dark-green, green, and orange lines indicate the mass fractions of ${}^4\text{He}$, ${}^{12}\text{C}$, ${}^{16}\text{O}$, ${}^{20}\text{Ne}$, ${}^{24}\text{Mg}$, Si-Sc, and Fe-peak elements (Ti-), respectively.

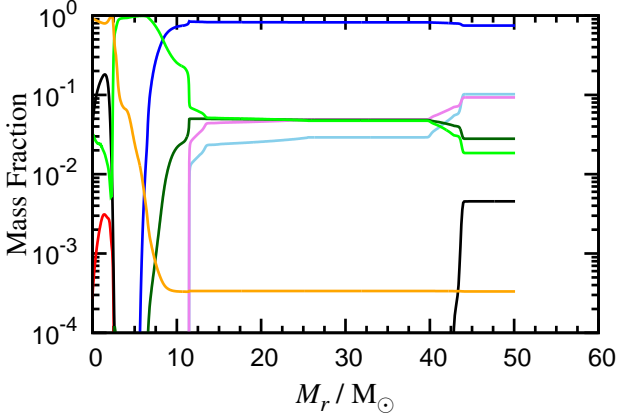


Figure 5. Mass fraction distribution of the $140 M_{\odot}$ model at the final time step. Red, black, sky-blue, blue, purple, dark-green, green, and orange lines indicate the mass fractions of ${}^1\text{H}$, ${}^4\text{He}$, ${}^{12}\text{C}$, ${}^{16}\text{O}$, ${}^{20}\text{Ne}$, ${}^{24}\text{Mg}$, Si-Sc, and Fe-peak elements (Ti-), respectively.

the mixing. This expansion reduces the stellar mass by $1.07 M_{\odot}$. The surface He mass fraction decreases to 0.13. The quasi-static contraction after the expansion continues for 98 d.

In the fourth pulsation, the central temperature reaches $\log T_{\text{C}} = 9.52$. Then, the expansion decreases to the temperature to $\log T_{\text{C}} = 9.03$. The central O-burning proceeds so that the Si core grows up to $4.3 M_{\odot}$ (see Fig. 4 (d)). This pulsation also expels the surface of $1.18 M_{\odot}$. The surface He mass fraction decreases to 0.07. The next quasi-static contraction continues for 102 d.

The fifth pulsation raises the central temperature up to $\log T_{\text{C}} = 9.59$. Then, the expansion decreases the central temperature to $\log T_{\text{C}} = 9.09$. The Si core grows up to 6.6

Table 2. The mass of the star or remnant M , ejecta mass M_{ej} , kinetic energy of ejecta E_{kin} , and time interval to the next pulse Δt_{pulse} or SN explosions for each pulse of the 140 , 200 , and $250 M_{\odot}$ models.

Pulse or SN	M (M_{\odot})	M_{ej} (M_{\odot})	E_{kin} (erg)	Δt_{pulse} (yr)
140 M_{\odot} model ($M = 54.09 M_{\odot}$ before PPI)				
First pulse	54.09	0.00	0.00	1.77×10^{-3}
Second pulse	53.84	0.25	1.26×10^{49}	4.69×10^{-2}
Third pulse	52.77	1.07	3.74×10^{49}	2.69×10^{-1}
Fourth pulse	51.59	1.18	3.83×10^{49}	2.79×10^{-1}
Fifth pulse	50.65	0.94	2.48×10^{49}	2.79×10^{-1}
Sixth pulse	50.10	0.55	2.99×10^{49}	4.32×10^{-2}
SN (10^{51} erg)	39.49	10.61	1.02×10^{51}	
SN (10^{52} erg)	1.95	48.12	9.71×10^{51}	
200 M_{\odot} model ($M = 58.65 M_{\odot}$ before PPI)				
First pulse	57.13	1.52	6.39×10^{49}	9.05×10^{-1}
Second pulse	55.08	2.05	5.62×10^{49}	2.03×10^1
Third pulse	54.38	0.70	1.93×10^{49}	5.34×10^{-2}
Fourth pulse	53.35	1.03	6.53×10^{49}	8.52×10^{-2}
SN (10^{51} erg)	41.82	11.53	9.97×10^{50}	
SN (10^{52} erg)	1.96	51.39	1.03×10^{52}	
250 M_{\odot} model ($M = 61.03 M_{\odot}$ before PPI)				
First pulse	60.48	0.55	2.90×10^{49}	1.10×10^{-1}
Second pulse	56.26	4.22	3.89×10^{50}	1.43×10^3
Third pulse	53.16	3.10	2.87×10^{50}	3.74
SN (10^{51} erg)	38.64	14.52	1.00×10^{51}	
SN (10^{52} erg)	1.98	51.779	1.08×10^{52}	

M_{\odot} through this pulsation (see Fig. 4 (e)). At the same time, about a half of the intermediate nuclei at the centre are burned into Fe-peak elements. The O- and Si-burnings at the central region expand the star. The envelope of 0.94

Table 3. The final mass M_f , Fe-core mass M_{Fe} , CO-core mass M_{CO} , the surface mass fractions of ^4He $X_S(^4\text{He})$, ^{12}C $X_S(^{12}\text{C})$, ^{16}O $X_S(^{16}\text{O})$, ^{20}Ne $X_S(^{20}\text{Ne})$, ^{24}Mg $X_S(^{24}\text{Mg})$, and ^{28}Si $X_S(^{28}\text{Si})$ at the final stage.

Model	M_f/M_\odot	M_{Fe}/M_\odot	M_{CO}/M_\odot	$X_S(^4\text{He})$	$X_S(^{12}\text{C})$	$X_S(^{16}\text{O})$	$X_S(^{20}\text{Ne})$	$X_S(^{24}\text{Mg})$	$X_S(^{28}\text{Si})$
140	50.10	2.57	43.51	4.5×10^{-3}	0.102	0.748	0.093	0.028	0.018
200	53.35	2.38	53.35	3.3×10^{-5}	0.084	0.765	0.093	0.036	0.013
250	53.16	2.10	53.16	1.9×10^{-5}	0.046	0.812	0.064	0.043	0.028

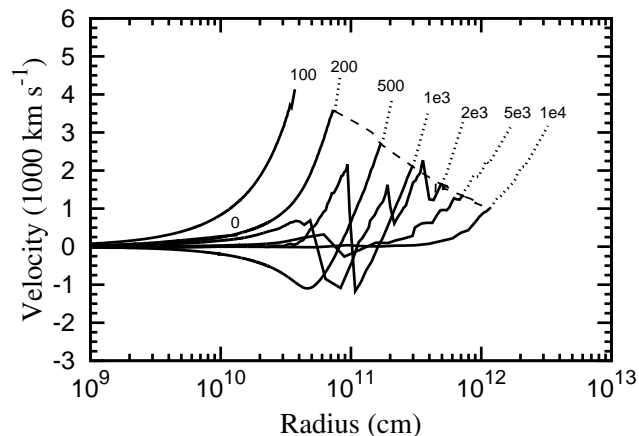


Figure 6. The time variation of the velocity distribution as a function of the radius during the fourth pulsation of the 140 M_\odot model. In each line, solid part indicates the gravitationally bounded region and dotted part indicates the unbound region, i.e., the velocity exceeds the escape velocity. The dashed line indicates the outer boundary of the bounded region. The number attached to each line denotes the time after the star has the maximum total energy in the pulsation.

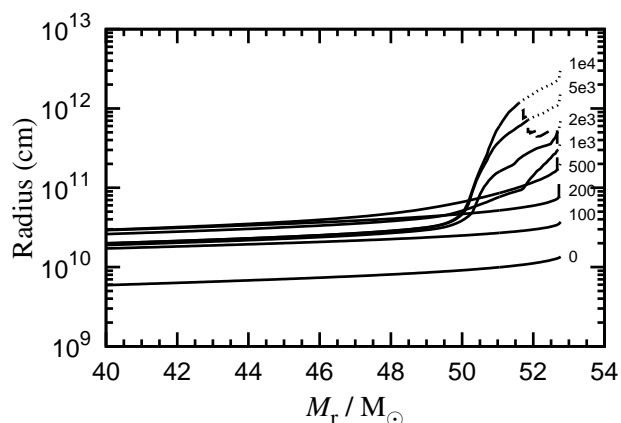


Figure 7. The time variation of the radius distribution as a function of the mass coordinate during the fourth pulsation of the 140 M_\odot model. In each line, solid part indicates the gravitationally bounded region and dotted part indicates the unbound region. The dashed line shows the outer boundary of the bounded region. The number attached to each line denotes the time after the star has the maximum total energy in the pulsation.

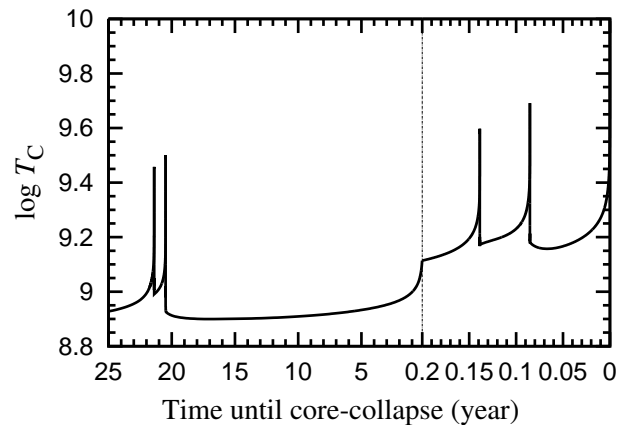


Figure 8. Time evolution of the central temperature $\log T_C$ of the 200 M_\odot model during the PPI stage. The scale of the horizontal axis changes at 0.2 yr, which is indicated by the vertical dashed line.

M_\odot is lost by the expansion and He mass fraction at the surface decreases to 0.02. The next quasi-static contraction continues for 102 d.

In the sixth pulsation, the central temperature becomes $\log T_C = 9.68$. This pulsation expands the star until the central temperature becomes $\log T_C = 9.20$. This high temperature induces the core Si-burning and a 2.3 M_\odot Fe core is formed (see Fig. 4 (f)). The Si and O/Si layers are also formed outside the core. This expansion expels the outer region of 0.55 M_\odot . The surface He mass fraction decreases to 4.5×10^{-3} . Thus, the surface He mass fraction becomes much smaller than that before the PPI stage.

The next contraction does not change to expansion, and the central core gravitationally collapses. Quasistatic contraction continues for 16 d and gradually changes to the dynamical collapse. Fig. 5 is the mass fraction distribution at the final step of the 140 M_\odot model. The Fe-core mass is 2.6 M_\odot and the Si-layer extends to 8.3 M_\odot . This star loses the outer region of 3.99 M_\odot during the pulsations. He mass fraction at surface decreases to 4.5×10^{-3} and a small amount of He injects into inner region by the mixing. The final CO-core mass is 43.51 M_\odot . The final mass, Fe-core mass, CO-core mass, the surface mass fractions of ^4He , ^{12}C , ^{16}O , ^{20}Ne , ^{24}Mg , and ^{28}Si are listed in Table 3. Note that the Fe core mass is defined as the largest mass coordinate satisfying the mass fraction of Fe-peak elements larger than 0.5.

We explain the mass ejection by the PPI of the 140 M_\odot model. We present the motion of outermost region during the fourth pulsation of the 140 M_\odot model. Fig. 6 shows the time evolution of the velocity distribution in the range of

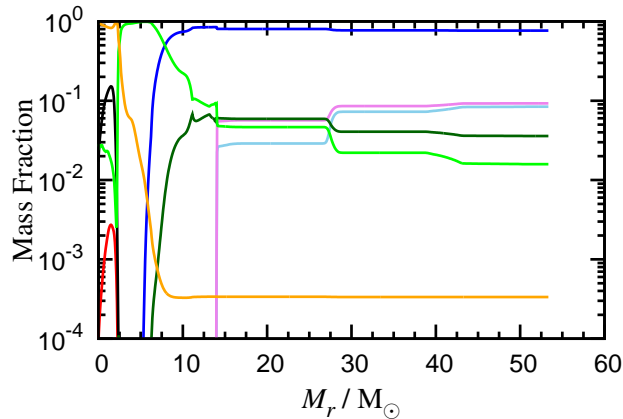


Figure 9. Same as Fig. 5, but for the 200 M_{\odot} model.

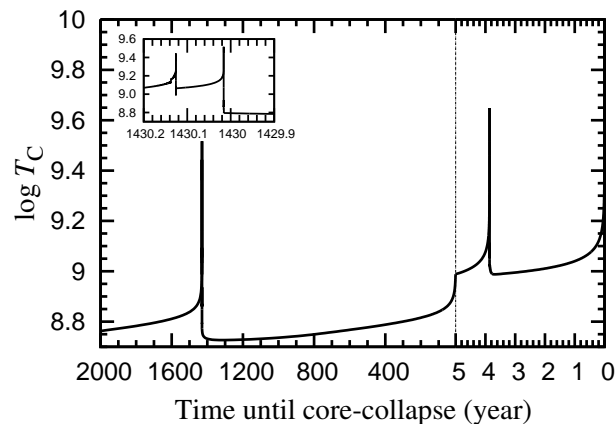


Figure 10. Time evolution of the central temperature $\log T_C$ of the 250 M_{\odot} model during the PPI stage. The scale of the horizontal axis changes at 5 yr, which is indicated by the vertical dashed line. The small figure shows the central temperature between 1430.2 yr and 1429.9 yr.

$r \geq 10^9$ cm. First, the velocity in this region is less than 1000 km s^{-1} and the materials accelerate outwards. The velocity increases for hundreds second, and the velocity of the surface material exceeds the escape velocity at ~ 200 s. Then, the stellar interior starts contracting and the contraction motion gradually propagates outwards. However, the surface materials continue to expand. As a result, the unbound region gradually moves outward. After several thousand seconds, the unbound surface expands with a constant velocity with ~ 3200 km s^{-1} . On the other hand, most bounded material contracts slowly. Finally, the kinetic energy of the ejecta in this pulsation is 3.83×10^{49} erg.

Fig. 7 shows the time evolution of the radius as a function of mass coordinate in outer region ($M_r \geq 40 M_{\odot}$) during the fourth pulse. First, the outer region expands for ~ 500 s. Then, the contraction motion propagates to the outer region and the expanding region gradually turns into the contraction. The contraction proceeds very slowly so the radial distribution of the contraction region changes quasi-statically. The region with $M_r \lesssim 50 M_{\odot}$ does not change the radial distribution after about 2000 s. On the other hand, the re-

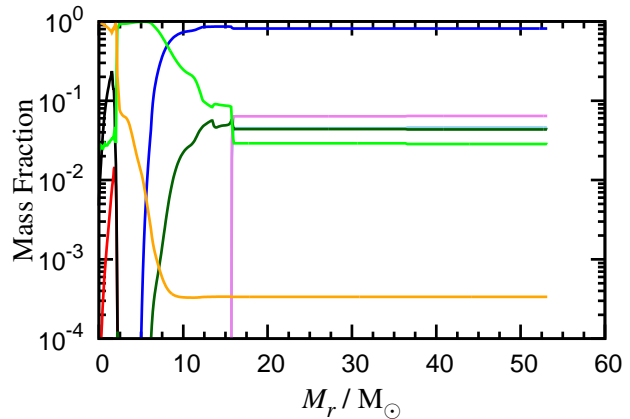


Figure 11. Same as Fig. 5, but for 250 M_{\odot} model. The line of the ^{12}C mass fraction in $M_r \geq 16 M_{\odot}$ almost overlaps with that of ^{24}Mg .

gion with $M_r \gtrsim 51 M_{\odot}$ still expands and the outer boundary of the bound region shifts inward until $\sim 10^4$ s. Finally, the outer boundary becomes $51.59 M_{\odot}$.

2.3 Stellar mass dependence

Properties of pulsations induced by PPI depend on the CO-core mass before the PPI stage. Here, we show the properties of the pulsations during PPI stages in the 200 and 250 M_{\odot} models and compare with the 140 M_{\odot} model. Table 2 shows the stellar mass, ejecta mass, kinetic energy of the ejecta, and time interval from the previous pulse in each pulse.

2.3.1 200 M_{\odot} model

Fig. 8 shows the time evolution of the central temperature of the 200 M_{\odot} model during the PPI stage. This model pulsates four times for about 22 yr before CC. The contraction period after the second pulsation is 20.3 yr. This period is much longer than that of other pulsations. The second pulsation also causes the lowest minimal central-temperature among the pulsations.

The mass ejection of the 200 M_{\odot} model is also presented in Table 2. The ejected mass during each pulse is 0.70–2.05 M_{\odot} . The second pulsation has ejected the largest mass. The second pulsation also induced the longest quasi-static contraction after the expansion. So, this pulsation seems to be the strongest pulsation. The kinetic energy of the ejecta is $(1\text{--}4) \times 10^{49}$ erg in each pulse. The mass of $5.30 M_{\odot}$ is lost by the pulsations and the total mass finally becomes $53.35 M_{\odot}$.

Fig. 9 shows the mass fraction distribution just before the CC. The Fe core with $2.38 M_{\odot}$ forms after the PPI stage. The surrounding Si-rich layer extends to $7.84 M_{\odot}$. The layer outside the Si-rich layer is O-rich. The O-rich layer extends from about $4 M_{\odot}$. The second abundant element depends on the mass coordinate. The mixing during the PPI stage raises the abundances of Si, Mg, and Ne. The surface He has been lost during the PPI stage and the surface composition mainly consists of O, C, and Ne. He mass fraction at the surface is 3.3×10^{-5} .

We obtained four pulsations during the PPI stage in the 200 M_{\odot} model. The number of pulsations is smaller than the 140 M_{\odot} model. On the other hand, the period of the PPI stage is much longer. The total ejected mass is 5.30 M_{\odot} , which is also larger than that of the 140 M_{\odot} model. Thus, the PPI of the 200 M_{\odot} model is stronger than that of the 140 M_{\odot} model. The larger CO core induces stronger contraction by PPI and stronger few pulses can produce Fe core effectively.

2.3.2 250 M_{\odot} model

Fig. 10 shows the time evolution of the central temperature of the 250 M_{\odot} model. This model pulsates three times during the PPI stage. In the first pulse, the central temperature rises to $\log T_C = 9.44$ and more than half of the central O is burned to Si and other intermediate nuclei. This pulse ejects the 0.55 M_{\odot} envelope. After 0.11 yr from the first pulse, the second pulsation occurs. The central temperature becomes $\log T_C = 9.52$ and the O in the central region of 0.39 M_{\odot} is burned. Then, whole of the star expands and the temperature decreases to $\log T_C = 8.73$. This expansion ejects 4.22 M_{\odot} outermost region with the kinetic energy of 3.9×10^{50} erg. This strong expansion also extends the contraction time of the star. It takes 1430 yr until the next pulsation. The third pulse raises the central temperature to $\log T_C = 9.65$. The Fe core with 0.84 M_{\odot} is formed and 3.10 M_{\odot} outer region is ejected.

Fig. 11 shows the mass fraction distribution of the 250 M_{\odot} model at the pre-SN stage. The Fe-core mass becomes 2.10 M_{\odot} in this model. It is smaller than that of the 200 M_{\odot} model. The strong expansion would prevent the growth of the Fe core. There is no He envelope. He mass fraction at surface is 2×10^{-5} . The O/Ne layer extends to the stellar surface. Almost all He in the outer region is lost during the second pulsation. The secondary main components are Ne, C, Mg, and Si. The mixing during the second and third pulsations makes the composition in the O/Ne layer homogeneous.

The 250 M_{\odot} model causes a smaller number of pulses, much longer PPI period, and larger mass ejection than the 200 M_{\odot} model. These trends are opposite to the 140 M_{\odot} model. We see from the above results that larger CO core model induces smaller number of pulses, longer PPI period, and larger mass ejection. Lower minimal temperature also correlates with a long pulse period. The large CO core induces stronger contraction. Stronger contraction causes stronger nuclear burning. The stronger nuclear burning brings about stronger expansion and larger mass ejection. It also produces more nuclear-burning product. The stronger expansion makes the bound of the star looser, so that the period until the next contraction becomes longer. Since more nuclear-burning product is synthesized in each pulsation, the number of pulses to form Fe core enough to collapse is smaller.

3 SN EXPLOSIONS

We calculate SN explosions after the CC of the stars using the PPM hydrodynamic code. We inject the explosion energy at $M_r = 2.0 M_{\odot}$. We consider two cases of the explosion

energy, $E_{51} = 1$ and 10, where E_{51} is the explosion energy in units of 10^{51} erg.

The final masses of the central remnant and the ejecta are listed in Table 2. In the explosion models of $E_{51} = 1$, most of the exploded materials do not reach the escape velocity and fall-back to the central remnant. The ejecta mass is about 10 M_{\odot} , which is much smaller than the progenitor mass, in the three models. Although ^{56}Ni is synthesized in the central region, it falls back to the central remnant and is not ejected.

In the explosion models with $E_{51} = 10$, all the materials outside the energy-injected region are ejected. We do not include α -network in the hydrodynamic calculation. So, we roughly estimate the ejected amount of ^{56}Ni , assuming that materials that experience temperature higher than 5×10^9 K become entirely ^{56}Ni . The obtained ^{56}Ni mass is 2, 1.5, and 1.2 M_{\odot} in the 140, 200, 250 M_{\odot} models, respectively. In these simulations, we do not adopt the ‘collapsed-core progenitor model’ in Yoshida, Okita & Umeda (2014) for simplicity. The ^{56}Ni mass of the collapsed-core model would be larger than that of the present model by a factor of 2 at most.

4 LIGHT CURVES

4.1 Calculation method

Adopting the pulsational-mass-loss histories and the final SN explosion models as calculated in §2.1, we compute bolometric light curves resulting from hydrodynamic interactions between different mass-loss shells and the final SN ejecta. The hydrodynamic evolution following the multiple ejections of the shells and SN ejecta is followed by a one-dimensional, adiabatic Eulerian hydrodynamic code (Maeda et al. 2002; Maeda 2013). The calculation starts with the injection of the first mass-loss shell, then when the time is elapsed to reach to the ejection of the second mass-loss shell (Table 1), the second shell is injected to the computational domain. This process is repeated until the final SN ejecta are injected to the computational domain.

In the hydrodynamic calculations, we follow evolution of tracer particles which are freshly injected with each shell. The kinetic energies of all the particles are tracked, which allows us to use equation (7) in Moriya & Maeda (2014) to evaluate the kinetic energy which may be dissipated and converted into radiation due to the interaction. We set parameter $\epsilon = 0.3$ in equation (8) in Moriya & Maeda (2014) which gives a fraction of the dissipated energy converted to radiation.

At each time step and position, we estimate the optical depth assuming that the interaction region is fully ionized and that the opacity is dominated by electron scatterings, i.e., $0.2 \text{ cm}^2 \text{ g}^{-1}$ in absence of hydrogen. This information of the optical depth is used to compute the diffusion time-scale which is then convolved with the energy generation rate in producing the light curve, as well as to compute the position of the photosphere. In general, we find that the diffusion time scale is shorter than the dynamical evolution time-scale, and the resulting delay is largely negligible. This justifies our procedure to calculate the light curve, where it is assumed that the diffusion time-scale is neg-

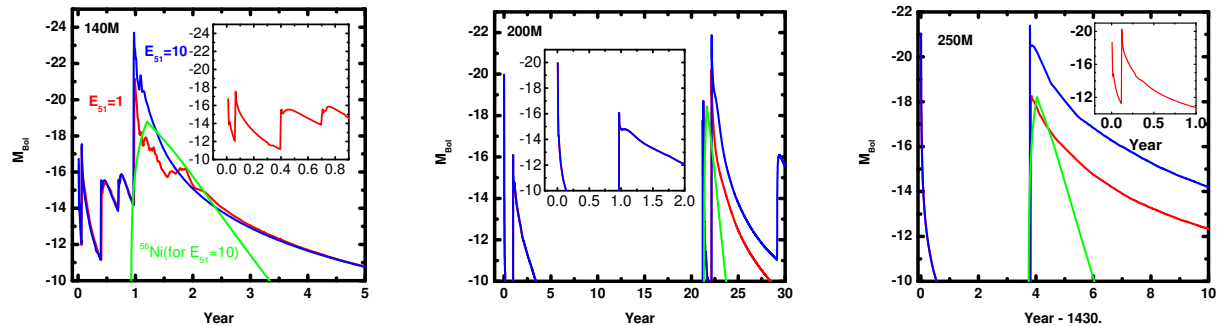


Figure 12. Bolometric light curves from the 140 (left), 200 (centre), and 250 M_{\odot} (right) models. The explosion energy of the final SNe is set to be $E_{51} = 1$ (red) and 10 (blue). In addition, the contribution from the decay of ^{56}Co , as originally produced as ^{56}Ni at the SN explosion, is indicated (green) for $E_{51} = 10$.

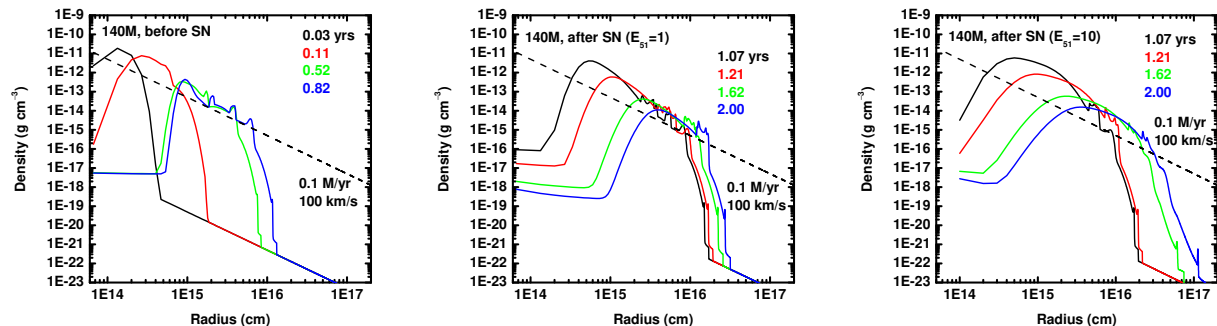


Figure 13. Evolution of the density profile for the 140 M_{\odot} model, before the SN (left), after the SN with $E_{51} = 1$ (centre), and after the SN with $E_{51} = 10$ (right). For comparison, the CSM density distribution expected from a steady-state mass-loss of $0.1 M_{\odot} \text{ yr}^{-1}$ with $v_w = 100 \text{ km s}^{-1}$, a typical value assumed for luminous SNe IIn and SLSNe, is shown by a dashed line.

ligible as compared to the dynamical time-scale (see e.g., Moriya & Maeda 2014).

The above treatment is only for the luminosity created by the hydrodynamic interaction. Another source of radiation is ^{56}Ni synthesized and ejected at the SN explosion. For the models with $E_{51} = 1$, virtually no ^{56}Ni is ejected by the SN, and therefore we neglect this contribution. For the models with $E_{51} = 10$, the following amount of ^{56}Ni is found to be ejected: $\sim 2 M_{\odot}$, $1.5 M_{\odot}$, and $1.2 M_{\odot}$ for the 140 M_{\odot} , 200 M_{\odot} , and 250 M_{\odot} models, respectively. For these models, we estimate the luminosity powered by the ^{56}Co decay following simple analytic models from the early (e.g., Arnett 1982) to the late (e.g., Maeda et al. 2003) phases.

We emphasize that our simplified treatment of the light-curve calculation allows only the first-order estimate, and the applicability to observational data requires several considerations. First, our assumption of the conversion efficiency of 30 per cent is calibrated for SNe IIn within a dense CSM (Moriya & Maeda 2014). Generally, when the ambient density is low, the radiation does not reach to thermal emission (e.g., Chevalier & Irwin 2012), and the efficiency as determined by the efficiency of non-thermal electron acceleration is as low as ~ 1 per cent (Maeda et al. 2014). Furthermore, in such a situation a bulk of the radiated energy is either in radio or X-rays, not in the optical

wavelengths. Also, we neglect the radiation cooling feedback to hydrodynamics, motivated by previous studies where the adiabatic treatment provides a reasonable description of the shock wave dynamics for SNe IIn as calibrated by radiation-hydrodynamic simulations (Moriya et al. 2013, 2014).

4.2 Results

Fig. 12 shows the calculated bolometric light curves. Fig. 13 shows the hydrodynamic evolution of the systems for the 140 M_{\odot} model. The hydrodynamic evolution of the other progenitor models is qualitatively similar. Fig. 14 shows the position of the photosphere, as computed by the optical depth to electron scatterings in the shocked high temperature regions, for the 140 M_{\odot} and 200 M_{\odot} models. The system from the 250 M_{\odot} model turns out to be optically thin except for the first year following the first pulse.

Fig. 12 shows that the light curve reflects the successive ejections of the shells and the SN ejecta, and interactions between them. At the time of the SN explosion, the ambient density becomes high, at the level comparable to, or even higher than, the CSM created by a strong mass-loss with $\dot{M} \sim 0.1 M_{\odot} \text{ yr}^{-1}$ (see Fig. 13). This situation is similar to what is suggested for luminous SNe IIn and SLSNe reaching to $M_{\text{bol}} \sim -20$ or even brighter (e.g.,

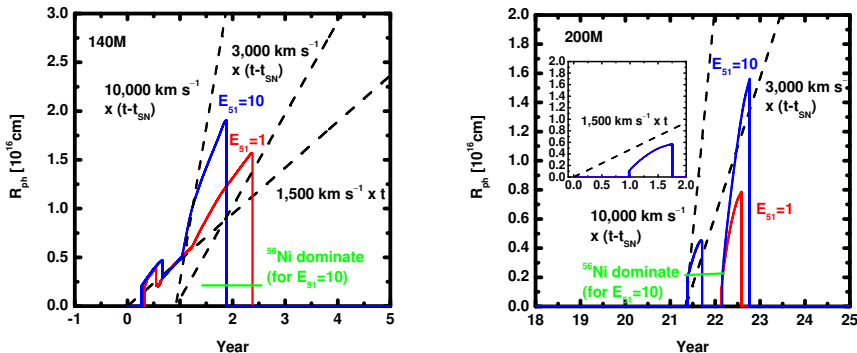


Figure 14. Evolution of the photospheric radius as determined by the optical depth to electron scatterings in the shocked high-temperature regions, as shown for the $140 M_{\odot}$ (left) and $200 M_{\odot}$ (right) models. The models with $E_{51} = 1$ are shown by a red line while the models with $E_{51} = 10$ are shown by a blue line. The period during which the ^{56}Co -decay-powered luminosity exceeds the interaction luminosity is indicated by a green line at the bottom.

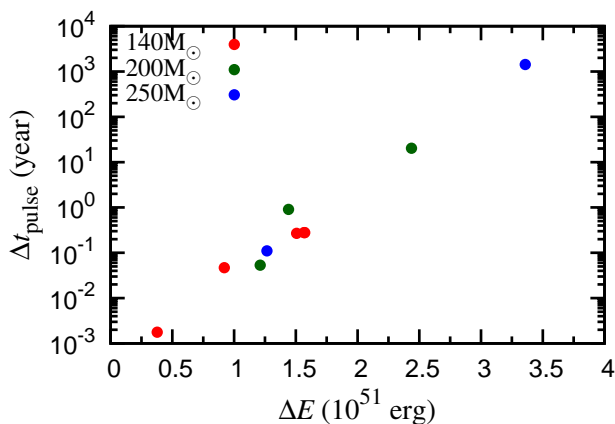


Figure 15. The relation between the energy difference ΔE and the time interval of pulsations Δt_{pulse} . Red, green, and blue points indicate the $140 M_{\odot}$, $200 M_{\odot}$, and $250 M_{\odot}$ models, respectively.

Moriya & Maeda 2014; Moriya et al. 2014). Indeed, we find that the calculated luminosities are similar to these events, or even brighter, reaching to $M_{\text{bol}} \sim -21$ ($E_{51} = 1$) or $M_{\text{bol}} \sim -23$ ($E_{51} = 10$) for the $140 M_{\odot}$ model, ~ -19 ($E_{51} = 1$) or ~ -21 ($E_{51} = 10$) for the $200 M_{\odot}$ model, and ~ -18 ($E_{51} = 1$) or ~ -20 ($E_{51} = 10$) for the $250 M_{\odot}$ model.

The difference in the shock-powered luminosity can be generally interpreted by the difference in the time-scale between the final shell ejection and the SN explosion, and also in the temporal history of the shell ejections. The $250 M_{\odot}$ model has a relatively long gap between the final shell ejection and the SN explosion (3.74 yr), therefore the ambient density at the time of the SN explosion is much lower than the other cases. This leads to a lower luminosity in this model than the others. The shell ejection history is more complicated in the $140 M_{\odot}$ model than the $200 M_{\odot}$ model, and thus the deceleration of these pulses is more important in the former. Therefore, the higher density ambient material is created for the $140 M_{\odot}$ model, leading to the higher luminosity. Related to this, many ‘pre-SN precursors’ are

seen in the $140 M_{\odot}$ model within a time-scale of a year, while the light curves of the other progenitor models are less complicated.

The light curves are mainly powered by the interaction, but the contribution from the decay of ^{56}Co (as initially produced as ^{56}Ni at the SN explosion) can be significant. For the explosion energy of $E_{51} = 10$, a substantial amount of ^{56}Ni ($\sim 1\text{--}2 M_{\odot}$) is created. In the $140 M_{\odot}$ model, indeed the ^{56}Co -decay power can exceed the interaction power, at a few months after the SN explosion and thereafter. Namely, we predict that the SN resulting from our scenario can change the properties and appearance according to the change in the power source, and in this case we predict that initially the SN should show signatures of strong interaction but later on it will look like SNe Ib/c. Note that the shocked region is optically thick even in the ^{56}Co -power dominating phase, thus it may look like different from typical SNe Ib/c in having an optically thick, electron-scattering dominated atmosphere. In the $200 M_{\odot}$ model, on the other hand, the ^{56}Co -decay power can dominate initially before the interaction develops strongly. In this case, the ^{56}Co -decay power may lead to a bright precursor having a character of typical SNe Ib/c, then a bright SN powered by the interaction follows.

5 DISCUSSION

5.1 Energy loss during PPI stage

We discuss time intervals and strength of pulsations. We find from Figs. 3, 8, and 10 that if the minimal temperature in each pulse is lower, the time interval is longer. In each pulse, a star is most loosely bound when the central temperature has a minimal value. We define the total energy at the minimal central temperature to be $E(T_{\text{min}})$. Then, the star gradually contracts and, at the same time, the energy is carried away by neutrinos. When the star dynamically contracts and just before rapid nuclear burning starts, the total energy of the star should have a minimal value E_{min} . We investigate the relation of the energy difference $\Delta E = E(T_{\text{min}}) - E_{\text{min}}$ to the time interval of pulsations Δt_{pulse} . Fig. 15 shows the relation between the energy difference ΔE and the time inter-

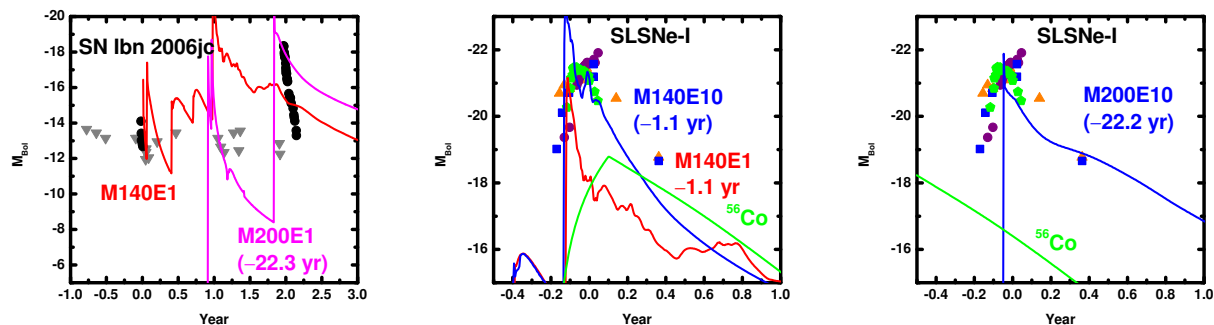


Figure 16. Some comparisons between our model light curves with SNe: the R -band light curve of SN Ibn 2006jc (Pastorello et al. 2007) as compared to the bolometric light curves from models $140 M_{\odot}$ ($E_{51} = 1$) and $200 M_{\odot}$ ($E_{51} = 1$) for left-hand panel, the R -band light curves of SLSNe-I (orange-triangles: PTF09atu, purple-circles: PTF09cnd, blue-squares: PTF09cwl, green-pentagons: PTF10cwr, in Quimby et al. 2011) as compared to the bolometric light curves for the $140 M_{\odot}$ model ($E_{51} = 1$ and 10) for center panel, and the $200 M_{\odot}$ model (with $E_{51} = 10$) for right-hand panel. For the models with $E_{51} = 10$, the contribution of ^{56}Co decay is shown by a green line. The models with $E_{51} = 1$ are shown by a red line while those with $E_{51} = 10$ are shown by a blue line, except for the $200 M_{\odot}$ model in the left-hand panel (shown by a magenta line).

val Δt_{pulse} . Although the stellar-mass dependence is unclear, the time interval strongly depends on ΔE . Strong temperature dependence of the neutrino-cooling rate brings about the shown dependence. We also see a rough correlation between ΔE and the ejected mass. The energy difference ΔE would be an indicator of the strength of pulsations.

In our calculations, the first pulsation seems to be weak for all models. In the 200 and $250 M_{\odot}$ models, the second pulsation is the strongest. This trend is somewhat different from the results in the supplementary information of Woosley, Blinnikov, & Heger (2007). They showed that the He star models with $M_{\text{He}} \geq 54 M_{\odot}$ indicated the longest time interval in the first pulsation. Typical kinetic energy of ejecta in our models seems to be smaller than that of them. We have not found a reason of the difference. The kinetic energy may relate to the time evolution of the density structure during pulsations complicatedly. We do not see a clear relation between the kinetic energy of ejecta and the pulse interval. Our models do not have the He-rich envelope. The CO-rich envelope may be bound stronger than the envelope of He-star models.

5.2 Implications for luminous SNe

For an illustration purpose, we compare our bolometric light curves with the R -band light curves of some SNe in Fig. 16. Since our model is essentially hydrogen-free, we restrict the comparison to a class of SNe Ib/c for which the hydrodynamic interaction has been suggested to be a source of the luminosity (among several other interpretations). The comparison includes the following SNe: (1) SN Ibn 2006jc as a prototypical SN showing the strong interaction between the SN ejecta and H-free environment (Pastorello et al. 2007; Anupama et al. 2009) (but see Tominaga et al. 2008, for different interpretation), and (2) SLSNe-I, which are characterized by a huge luminosity exceeding $M_R \sim -21$ and by H-free spectra (Quimby et al. 2011; Gal-Yam 2012), for which not only the progenitor system but also the emission process have not been clarified yet (e.g., a magnetar-powered model Kasen & Bildsten 2010) (see also Maeda et al. 2007). Note

that SLSNe-I do not show obvious spectrum signatures of interaction, but how the interaction between the SN ejecta and H/He-poor CSM manifests itself in spectra has not been clarified: it may not necessarily show obvious strong emission lines (Sorokina et al. 2015).

The models do not well reproduce the light curve of SN 2006jc. The time-scale of 2 yr between the precursor and the SN explosion is roughly right as the time-scale expected for the pulsational activities in the $140 M_{\odot}$ or $200 M_{\odot}$ progenitor. Also, the peak luminosity is roughly consistent, for $E_{51} = 1$, to the observed one, which means that the PPISN model can provide the environment similar to that around SN 2006jc without fine-tuning. However, the model light curve after the SN decays much slower than the observations, which is also another indication of properties of the environment. There is thus a difficulty to explain the relatively rapid decay as seen in SN 2006jc by the PPISN model.

As for SLSNe-I, the explosion energy as large as $E_{51} = 10$ is required to explain the luminosity and duration of these SNe, as expected. While details are not fitted by our models, these models provide qualitatively good similarity to the observed light curves. For both $140 M_{\odot}$ and $200 M_{\odot}$ models, the luminosity and decay time-scale are explained reasonably well, without any fine-tuning. Another interesting property is seen in the $140 M_{\odot}$ model. In this model, the ^{56}Co -decay dominates the power input from ~ 3 months after the explosion, and then the SN should look like a SN Ib/c. Indeed, at least some SLSNe-I with such late-time observations available, they show spectra similar to SNe Ib/c (Quimby et al. 2011; Nicholl et al. 2014; Chen et al. 2015). We also note that while the CSM interaction is disfavoured as a model for some SLSNe-I based on a rapidly decaying model light curve as compared to observations (Nicholl et al. 2014), the PPISN model could evolve more slowly than a fiducial interaction model either owing to the contribution by the ^{56}Co power ($140 M_{\odot}$; see centre panel of Fig. 16) or owing to a complicated pre-SN CSM structure ($200 M_{\odot}$; see right-hand panel of Fig. 16).

The $140 M_{\odot}$ model also predicts the pre-SN activities at

the level of $M_{\text{bol}} \sim -16$, which happen several times in 1 yr time-scale. Leloudas et al. (2012) found a probable precursor in SLSN-I 2006oz, at 6–10 d before the beginning of the main part of the light curve, or ~ 30 –40 d before the peak luminosity. The time-scale may be consistent with our model, while the luminosity of the precursor (~ -19 mag) far exceeds our model prediction (~ -16 mag). Details will be sensitive to the progenitor mass, and further investigation for different mass is required. In any case, within our scenario we generally expect a larger number of multiple pre-SN outbursts for a brighter SN (linked by the density of the environment), and SLSNe-I following this path, if they exist, should show such activities. Therefore, future observations to catch pre-SN outbursts are important to discriminate our models from various proposed models for SLSNe-I. For SLSNe-I at the redshift of $z = 0.2$, the pre-SN outburst of the $140 M_{\odot}$ model should reach to an apparent magnitude of $m_{\text{bol}} \sim 24$, thus this can be investigated by surveys with 4m-class telescopes. Typical sensitivities by surveys with 8m-class telescopes (e.g., Subaru/HSC, LSST) will be sufficient for the detection of such outbursts up to $z \sim 0.5$ –0.6. For example, the ongoing Subaru/HSC-deep survey is expected to detect ~ 10 SLSNe below $z \sim 1$ (Tanaka et al. 2012), and it is designed to visit the same field twice a month for continuous 3 months. With this cadence we could detect at least the outburst following the ejection of the final shell before the SN explosion (Figs. 12 and 16).

If a very massive star collapses and does not explode after the PPI stage, only precursor events before the collapse could be observed. In the $140 M_{\odot}$ model, multiple peaks with $M_{\text{bol}} \sim -16$ could be observed in the light curve (see the left-hand panel of Fig. 12). This feature may be similar to the precursor of SN 2006jc. Two luminous events with $M_{\text{bol}} \sim -16$ and -18 will be observed in the interval of ~ 20 yr for the $20 M_{\odot}$ model. The $250 M_{\odot}$ model will give a luminous event achieving $M_{\text{bol}} \sim -20$. If a strong pulsation occurs like the 200 and $250 M_{\odot}$ models, the luminosity of the luminous event by the interaction can be luminous and could achieve that of an SLSN.

Recently, an SLSN-I showing $H\alpha$ emissions in its late-time spectra has been observed. The SN, iPTF13ehe, was observed as an SLSN-I and its light-curve has typical SLSN-R features (Yan, et al. 2015). They considered that the broad $H\alpha$ emission line that appeared in late phases is formed by the interaction between SN ejecta and the $< 30 M_{\odot}$ H-rich CSM shell, which has been ejected by the PPI. They also modelled the nebular spectra, which suggest $M(^{56}\text{Ni}) \sim 2.5 M_{\odot}$. Such a large amount of ^{56}Ni production accompanying the PPI is possible only by an energetic SN explosion induced by the CC of an Fe core in a massive CO core. This observational feature could suggest that substantial ^{56}Ni ejection is indeed possible by an energetic CCSN from a massive CO core as discussed in Umeda & Nomoto (2008), Yoshida, Okita & Umeda (2014) and this study.

A possibility of strong X-ray emissions from the interaction between the SN forward shock and dense CSM (due to pulsational mass-loss) has been investigated by Pan et al. (2013). In our 140 and $200 M_{\odot}$ models, the strong interaction takes place at $R \sim 10^{16}$ cm, and thus the interacting region is optically thick, forming a photosphere (see Fig. 14). This is in accordance with the estimate by Pan et al. (2013). In this case, most of the emitted X-rays will be converted

into optical emission within the interaction region. Still, the region immediately behind the forward shock can be optically thin avoiding thermalization, and thus a fraction of the luminosity may be emitted in X-rays. This will be negligible as compared to the optical luminosity, but could still be considered as a strong X-ray emitter given by the large bolometric luminosity. For the $250 M_{\odot}$ model, indeed the interacting region is optically thin to electron scatterings for most of the time. Therefore, it is possible that a large fraction of the luminosity would be emitted as X-rays. However, the ejecta will still be optically thick (which we did not take into account in our simulations), and will convert about a half of the X-ray to optical emission. Therefore, in this case the SN could be a very strong X-ray emitter, but still will not change our result about the optical luminosity significantly. In any case, it is possible that the PPI SNe could be luminous in X-rays and possibly be observed in the high energy emission.

6 SUMMARY

We investigated the evolution of the 140 , 200 , and $250 M_{\odot}$ models with $Z = 0.004$, which had become 54.1 , 58.7 , and $61.0 M_{\odot}$ after the C-burning, including mass ejection induced by PPI. Then, we calculated SN explosions with two cases of explosion energy. We also calculated light curves created by the interaction of the CSMs ejected by the PPI and that between the CSM and the SN ejecta. The obtained light curves were applied to optically luminous transients. We summarize the main results as follows.

The 140 , 200 , and $250 M_{\odot}$ models experienced six, four, and three pulsations during the PPI stage. A part of the outer envelope exceeded the escape velocity and, thus, ejected from the stars. The final stellar masses of these models are 50.10 , 53.35 , and $53.16 M_{\odot}$.

The surface composition changes by the mass ejection during the PPI stage. The final He mass fraction at the surface is $\sim 2 \times 10^{-3}$ for the $140 M_{\odot}$ model and much smaller for the other two models. If these stars explode, they will be observed as SNe Ic.

Larger CO-core model experiences the PPI stage with fewer pulsation numbers and longer period. This trend is consistent with the result in Woosley, Blinnikov, & Heger (2007). The PPI period is almost determined by the strongest pulsation in the 200 and $250 M_{\odot}$ models.

The interactions of the PPI ejecta with the CSM formed by previous ejections make optically luminous transients. The $140 M_{\odot}$ model reaches $M_{\text{bol}} \sim -16$ to -18 for several times. The 200 and $250 M_{\odot}$ models become bright up to $M_{\text{bol}} \sim -18$ and -20 , respectively, even without an energetic SN. If an SN follows the CC, then the luminosities produced by the interactions of the CSM and the SN ejecta are higher than those of the CSM interactions. The obtained luminosities become comparable to SLSNe-I.

Although there are still difficulties such as reproducing short SN decay time, the CSM interaction during the PPI stage and the following SN could be tested by light curves of SLSNe-I in future surveys.

ACKNOWLEDGEMENTS

We thank Tony Pan for useful comments on X-ray emission from PPI SNe. This work has been partly support by the grants-in-aid for Scientific Research (24244028, 26400271, 26800100) from the MEXT of Japan and WPI Initiative, MEXT, Japan.

REFERENCES

- Anupama, G. C., Sahu, D. K., Gurugubelli, U. K., Prabhu, T. P., Tominaga, N., Tanaka, M., Nomoto, K. 2009, MNRAS, 392, 894
- Arnett, W. D. 1982, ApJ, 253, 785
- Chatzopoulos, E., Wheeler, J. C. 2012, ApJ, 760, 154
- Chen, T.-W., et al. 2015, MNRAS, 452, 1567
- Chevalier, R. A., & Irwin, C. M. 2012, ApJ, 747, L17
- Colella, P., Woodward, P. R. 1984, J. Comput. Phys., 54, 174
- Crowther, P. A., Schnurr, O., Hirschi, R., Yusof, N., Parker, R. J., Goodwin, S. P., Kassim, H. A. 2010, MNRAS, 408, 731
- Gal-Yam, A. 2012, Science, 337, 927
- Gal-Yam, A., et al. 2009, Nature, 462, 624
- Heger, A., & Woosley, S. E. 2002, ApJ, 567, 532
- Kasen, D. & Bildsten, L. 2010, ApJ, 717, 245
- Langer, N., Norman, C. A., de Koter, A., Vink, J. S., Cantiello, M., Yoon, S.-C. 2007, A&A, 475, L19
- Leloudas, G., et al. A&A, 541, A129
- Maeda, K. 2013, ApJ, 762, 14
- Maeda, K., Nomoto, K., Nakasato, N., Suzuki, T. 2002, in Slane P. O., Gaensler B. M., eds, ASP Conf. Ser. Vol. 271, Neutron Stars in Supernova Remnants. Astron. Soc. Pac., San Francisco, p. 379
- Maeda, K., Mazzali, P. A., Deng, J., Nomoto, K., Yoshii, Y., Tomita, H., Kobayashi, Y. 2003, ApJ, 593, 931
- Maeda, K., et al. 2007, ApJ, 666, 1069
- Maeda, K. Katsuda, S., Bamba, A., Terada, Y., Fukazawa, Y. 2014, ApJ, 785, 95
- Moriya, T., Maeda, K. 2014, ApJ, 790, L16
- Moriya, T. J., Maeda, K., Taddia, F., Sollerman, J., Blinnikov, S. I., Sorokina, E. I. 2013, MNRAS, 435, 1520
- Moriya, T. J., Maeda, K., Taddia, F., Sollerman, J., Blinnikov, S. I., Sorokina, E. I. 2014, MNRAS, 439, 2917
- Moriya, T., Tominaga, N., Tanaka, M., Maeda, K., Nomoto, K. 2010, ApJ, 717, L83
- Nicholl, M., et al. 2014, MNRAS, 444, 2096
- Pan, T., Patnaude, D., Loeb, A. 2013, MNRAS, 433, 838
- Pastorello, A., et al. 2007, Nature, 447, 829
- Pastorello, A., et al. 2013, ApJ, 767, 1
- Quimby, R. M., Aldering, G., Wheeler, J. C., Höflich, P., Akerlof, C. W., Rykoff, E. S. 2007, ApJ, 668, L99
- Quimby, R. M., et al. 2011, Nature, 474, 487
- Smith, N., et al. 2007, ApJ, 666, 1116
- Sorokina, E., Blinnikov, S., Nomoto, K., Quimby, R., Alexey T. 2015, ApJ, submitted (arXiv:1510.00834)
- Takahashi, K., Yoshida, T., Umeda, H., Sumiyoshi, K., Yamada, S. 2015, MNRAS, 456, 1320
- Tanaka, M., Moriya, T. J., Yoshida, N., Nomoto, K. 2012, MNRAS, 422, 2675
- Tominaga, N., et al. 2008, ApJ, 687, 1208
- Umeda, H., Nomoto, K., 2002, ApJ, 565, 385
- Umeda, H., Nomoto, K. 2005, ApJ, 619, 427
- Umeda, H., Nomoto, K. 2008, ApJ, 673, 1014
- Waldman, R. 2008, ApJ, 685, 1103
- Woosley, S. E., Blinnikov, S., Heger, A. 2007, Nature, 450, 390
- Yan, L., et al. 2015, ApJ, 814, 108
- Yoshida, T., Okita, S., Umeda, H. 2014, MNRAS, 438, 3119
- Yoshida, T., Umeda, H. 2011, MNRAS, 412, L78
- Yungelson, L. R., van den Heuvel, E. P. J., Vink, J. S., Portegies Zwart, S. F., de Koter, A. 2008, A&A, 477, 223
- Yusof, N., et al. 2013, MNRAS, 433, 1114

This paper has been typeset from a \TeX / \LaTeX file prepared by the author.